Buoyant Motion of a Turbulent Thermal

NATHANIEL TARSHISH

Atmospheric and Oceanic Sciences Program, Princeton University, Princeton, New Jersey

NADIR JEEVANJEE

Department of Geosciences, Princeton University, Princeton, New Jersey

DANIEL LECOANET

Princeton Center for Theoretical Science, Princeton University, Princeton, New Jersey

(Manuscript received 30 November 2017, in final form 2 June 2018)

ABSTRACT

By introducing an equivalence between magnetostatics and the equations governing buoyant motion, we derive analytical expressions for the acceleration of isolated density anomalies (thermals). In particular, we investigate buoyant acceleration, defined as the sum of the Archimedean buoyancy B and an associated perturbation pressure gradient. For the case of a uniform spherical thermal, the anomaly fluid accelerates at $2B/3$, extending the textbook result for the induced mass of a solid sphere to the case of a fluid sphere. For a more general ellipsoidal thermal, we show that the buoyant acceleration is a simple analytical function of the ellipsoid's aspect ratio. The relevance of these idealized uniform-density results to turbulent thermals is explored by analyzing direct numerical simulations of thermals at a Reynolds number (Re) of 6300. We find that our results fully characterize a thermal's initial motion over a distance comparable to its length. Beyond this buoyancy-dominated regime, a thermal develops an ellipsoidal vortex circulation and begins to entrain environmental fluid. Our analytical expressions do not describe the total acceleration of this mature thermal, but they still accurately relate the buoyant acceleration to the thermal's mean Archimedean buoyancy and aspect ratio. Thus, our analytical formulas provide a simple and direct means of estimating the buoyant acceleration of turbulent thermals.

1. Introduction

Buoyancy is the root cause of thermal convection in the atmosphere and fundamentally governs the vertical acceleration of clouds. A density anomaly's buoyancy is most often characterized by the Archimedean formula $B = -\rho'/\rho_o g$. However, only an *infinitesimal* buoyant parcel, whose motion has a negligible impact on the environment, actually accelerates at its familiar Archimedean value. A density anomaly of finite size disrupts its environment and sets the surrounding fluid in motion. This loss of momentum to the environment reduces the finite parcel's buoyant acceleration from its Archimedean buoyancy to its "effective buoyancy" β, as introduced by Davies-Jones (2003) and discussed by Doswell and Markowski (2004), Xu and Randall (2001), and Krueger et al. (1995). The back reaction exerted by the environment on the buoyant fluid is realized by a buoyancy perturbation pressure (to be fully defined in the next section).

The reduction from B to β is determined by the geometry of the density anomaly. As discussed in Houze (2014), for broad pancake-shaped density anomalies, buoyant motion is severely inhibited by the surrounding fluid, and β can be several orders of magnitude less than B. On the other hand, narrow pencil-shaped density anomalies impart negligible momentum to their environment, and B serves as a reliable proxy for β.

Moving beyond this qualitative understanding, approximate formulas and scalings exist for the effective buoyancy in updrafts (Morrison 2016a,b; Peters 2016), of an isolated bubble (Pauluis and Garner 2006), and in hydrostatic versus nonhydrostatic models (Weisman et al. 1997; Jeevanjee 2017). Furthermore, exact analytical results for the effective buoyancy along the central axis of a buoyant cylinder were obtained by

Corresponding author: Nathaniel Tarshish, tarshish@noaa.gov

DOI: 10.1175/JAS-D-17-0371.1

Jeevanjee and Romps (2016). While this progress is significant, we still lack a full 3D analytical solution for the effective buoyancy of a density anomaly even for idealized geometries, and thus have no quantitative picture for how the *environment* responds to buoyant accelerations.

Another issue is that convection schemes often account for the buoyancy perturbation pressure gradient by simply multiplying B by a fixed virtual (induced) mass coefficient. This coefficient is sometimes set equal to 2/3, which is the value for a solid sphere in potential flow (e.g., Romps and Charn 2015; Romps and Kuang 2010; Roode et al. 2012; Batchelor 2000). In a similar fashion, Turner (1964) approximated the perturbation pressure acting on an ellipsoidal thermal by appealing to the virtual mass coefficient of a solid ellipsoid. Not only does fixing a coefficient neglect the geometry-dependent nature of the buoyancy perturbation pressure, but there also does not seem to be any rigorous proof that the solid-body value is appropriate for a *fluid* density anomaly, which may experience an internal circulation and thus deform as it accelerates.

In this paper we aim to make progress on these questions by deriving the exact effective buoyancy for the idealized case of a uniformly buoyant ellipsoid. Our analytical results spring in part from the recognition of a novel mathematical equivalence between the equations of magnetostatics and effective buoyancy. We show that the magnetic field of a uniformly magnetized body of arbitrary shape is mathematically identical to the effective buoyancy of an identically shaped fluid density anomaly.

This equivalence allows us to leverage the long-standing classical literature on magnetization to find the effective buoyancy of an ellipsoidal thermal. In addition, the correspondence provides theoretical justification for appealing to the solid-body virtual mass coefficients in the case of ellipsoids, yet also proves that the connection between solid-body motion and fluid anomaly acceleration breaks down for all other geometries.

The relevance of the ellipsoidal geometry examined in this work is supported by the observed shapes of convecting thermals. The actively convecting cores of cumulus in large-eddy simulations (Sherwood et al. 2013; Romps and Charn 2015) and atmospheric observations (Damiani et al. 2006; Damiani and Vali 2007) are often ellipsoidal in shape. Laboratory experiments (e.g., Scorer 1957; Woodward 1959) of rising thermals also demonstrate this same ellipsoidal form.

Realistic turbulent thermals, of course, have nonuniform B fields. How relevant are theoretical formulas for β that assume uniform B? To answer this, we present simulations of a turbulent thermal and show that its *average* β can indeed be explained by our analytical formulas, when applied to the turbulent thermal's average B field.

2. Effective buoyancy preliminaries

We begin with the Boussinesq momentum equation,

$$\frac{D\mathbf{v}}{Dt} = -\frac{\nabla p'}{\rho_o} + B\mathbf{e}_z + \nu\nabla^2\mathbf{v}, \tag{1}$$

where $B = -\rho'/\rho_o g$ is the Archimedean buoyancy and ν is the molecular viscosity (Markowski and Richardson 2011). We decompose the pressure according to $p'(x, y, z, t) = p(x, y, z, t) - \overline{p(z)}$, where $\overline{p(z)}$ is in hydrostatic balance with the constant reference density ρ_o. Consider the divergence of the momentum equation,

$$\rho_o\frac{\partial}{\partial t}[\nabla\cdot\mathbf{v}] = -\rho_o\nabla\cdot(\mathbf{v}\cdot\nabla\mathbf{v}) - \nabla^2 p' + \rho_o\frac{\partial B}{\partial z} + \rho_o\nu\nabla^2(\nabla\cdot\mathbf{v}). \tag{2}$$

Boussinesq mass continuity ($\nabla\cdot\mathbf{v} = 0$) dictates that the total convergence tendency is zero, yielding a Poisson's equation for p',

$$\nabla^2 p' = -\rho_o\nabla\cdot(\mathbf{v}\cdot\nabla\mathbf{v}) + \rho_o\frac{\partial B}{\partial z}. \tag{3}$$

From this perspective the perturbation pressure arises to enforce mass continuity by opposing any convergence tendencies generated by advective motion or buoyancy.

The distinct physical mechanisms generating the perturbation pressure motivates further decomposing p' according to $p' = p_b + p_d$, where p_b is the buoyancy perturbation pressure driven statically by vertical gradients in the buoyancy field and p_d is the dynamic pressure generated by advective motion. The linearity of Poisson's equation then allows us to separate Eq. (3) into independent parts,

$$\nabla^2 p_b = \rho_o\frac{\partial B}{\partial z} \quad \text{and} \tag{4a}$$

$$\nabla^2 p_d = -\rho_o\nabla\cdot(\mathbf{v}\cdot\nabla\mathbf{v}). \tag{4b}$$

Likewise, the Lagrangian acceleration admits a complimentary decomposition. As in Jeevanjee and Romps (2015), we define the effective buoyancy β as the Lagrangian vertical acceleration that would result from instantaneously zeroing out the velocity field,

$$\beta = \left.\frac{Dw}{Dt}\right|_{\mathbf{v}\to 0} = -\frac{1}{\rho_o}\frac{\partial p_b}{\partial z} + B. \tag{5}$$

By accounting for p_b, the effective buoyancy is thus the true buoyant acceleration experienced by a finite-sized density anomaly.

We also define the dynamic acceleration as the Lagrangian acceleration that would result from instantaneously zeroing out the density anomaly field,

$$a_d = \left.\frac{Dw}{Dt}\right|_{\rho'\to 0} = -\frac{1}{\rho_o}\frac{\partial p_d}{\partial z} + \nu\nabla^2 w. \tag{6}$$

Together, the effective buoyancy and the inertial acceleration combine to give the Lagrangian vertical acceleration,

$$\frac{Dw}{Dt} = \beta + a_d. \tag{7}$$

Note that these definitions fully specify the boundary conditions necessary to determine p_b and p_d as detailed in Jeevanjee and Romps (2015).

Our focus in this article is on the effective buoyancy, but this is not to suggest that the dynamic acceleration is of little importance in atmospheric convection. In a mature thermal, the dynamic acceleration is comparable in magnitude to the effective buoyancy and is critical for establishing and maintaining the thermal's internal circulation. For the initial motion of a nascent thermal, however, the effective buoyancy dominates over the dynamic acceleration. In section 4, we further detail the transition between these two regimes.

3. Effective buoyancy of a spherical anomaly

We begin by seeking a solution for the effective buoyancy field of a spherical buoyancy anomaly of uniform Archimedean buoyancy B_o and radius R. In spherical coordinates centered on the buoyant sphere with $\mathbf{r} = (r, \varphi, \theta)$, polar angle θ, and azimuthal angle φ, the buoyancy field is described by

$$B(\mathbf{r}) = B_o H(R - r), \tag{8}$$

where $H(R-r)$ is the Heaviside step function. Relying on Eq. (4a), we compute the buoyancy perturbation pressure as

$$-\nabla^2 p_b = \rho_o B_o \cos\theta\, \delta(R - r), \tag{9}$$

where $\delta(R-r)$ is the Dirac delta function. Away from $r = R$, p_b solves Laplace's equation and thus admits a series solution in the spherical harmonics. The conditions that p_b be finite at $r = 0$ and vanish at infinity provide the piecewise expansion,

$$p_b(r,\theta) = \begin{cases} \sum_\ell a_\ell r^l P_\ell(\cos\theta), & r < R \\ \sum_\ell \frac{b_\ell}{r^{\ell+1}} P_\ell(\cos\theta), & r > R, \end{cases} \tag{10}$$

where P_ℓ is the ℓth member of the Legendre polynomials, which form a normalized basis for azimuthally symmetric functions on the sphere. For future reference, we note that $P_1(\cos\theta) = \cos\theta$ and $P_2(\cos\theta) = 1/2(3\cos^2\theta - 1)$. Dependence on φ is precluded by azimuthal symmetry (whereas θ symmetry is broken by gravity). To generate the boundary conditions, we multiply Eq. (9) by r^2 and separate $r^2\nabla^2$ into a radial and angular part,

$$\frac{\partial}{\partial r}\left(r^2\frac{\partial p_b}{\partial r}\right) + \nabla^2_{\text{ang}} p_b = -\rho_o B_o \cos\theta r^2 \delta(R - r), \tag{11}$$

where we have defined

$$\nabla^2_{\text{ang}} \equiv \frac{1}{\sin\theta}\frac{\partial}{\partial\theta}\left(\sin\theta\frac{\partial}{\partial\theta}\right) + \frac{1}{\sin^2\theta}\frac{\partial^2}{\partial\phi^2}. \tag{12}$$

Suppose p_b were discontinuous about $r = R$, then $\partial^2 p_b/\partial^2 r$ would generate a $\partial_r[\delta(R-r)]$ on the lhs of Eq. (11). Since the singularities on the lhs and rhs are now of different order {i.e., $\partial_r[\delta(R-r)]$ is linearly independent from $\delta(R-r)$}, we have a contradiction. Therefore, p_b is continuous.

Integrating Eq. (11) with respect to r over $[R-\varepsilon,\ R+\varepsilon]$ then yields

$$\lim_{\varepsilon\to 0}\left(\left.\frac{\partial p_b}{\partial r}\right|_{R+\varepsilon} - \left.\frac{\partial p_b}{\partial r}\right|_{R-\varepsilon}\right) = -\rho_o B_o \cos\theta, \tag{13}$$

where the angular term dropped out as $\varepsilon \to 0$, since p_b is continuous in r and smooth in θ.

Continuity of p_b provides that $b_\ell = a_\ell R^{2\ell+1}$, and we may write the expansion outside the spherical shell as

$$\sum_\ell \frac{a_\ell R^{2\ell+1}}{r^{\ell+1}} P_\ell(\cos\theta). \tag{14}$$

Enforcing the boundary condition (13) on the radial derivative gives

$$\lim_{\varepsilon\to 0}\sum_{\ell=1}^{\infty}\left[\frac{-(\ell+1)R^{2\ell+1}}{(R+\varepsilon)^{\ell+2}} - \ell(R-\varepsilon)^{\ell-1}\right] a_\ell P_\ell(\cos\theta) = -\rho_o B_o \cos\theta. \tag{15}$$

Recognizing $P_1(\cos\theta)$ on the rhs and invoking the linear independence of the Legendre polynomials demands that any factors in front of the $l \neq 1$ Legendre polynomials are individually zero,

$$\lim_{\varepsilon\to 0}\left[\frac{-(\ell+1)R^{2\ell+1}}{(R+\varepsilon)^{\ell+2}} - \ell(R-\varepsilon)^{\ell-1}\right] a_\ell = 0 \tag{16a}$$

$$\Rightarrow (2\ell+1)R^{\ell-1} a_\ell = 0. \tag{16b}$$

We find that $a_\ell = 0$ for $\ell \neq 1$. For the $\ell = 1$ case, we have

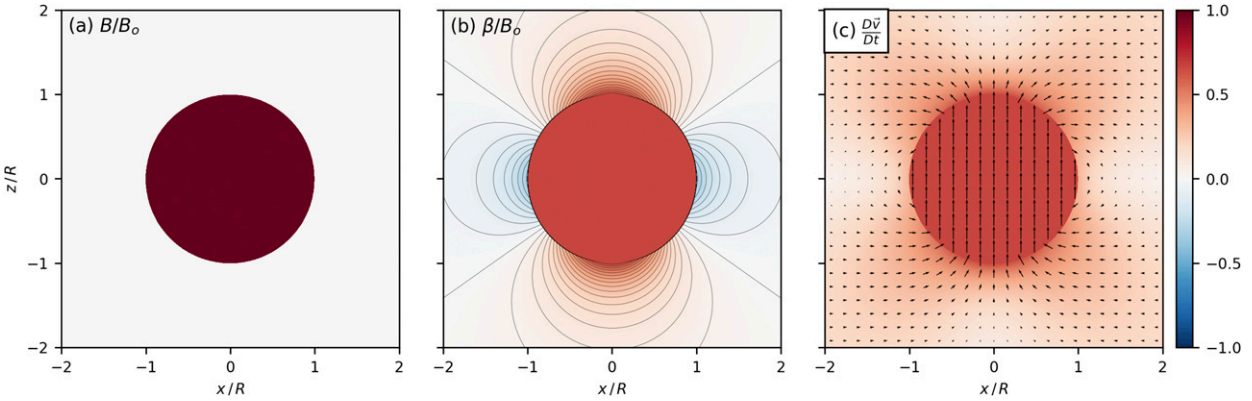

FIG. 1. A uniform spherical thermal: (a) vertical cross sections of the Archimedean buoyancy profile, (b) analytical solution for the effective buoyancy, and (c) analytical solution for the Lagrangian acceleration with vector acceleration (arrows) and acceleration magnitude (color).

$$\lim_{\varepsilon\to 0}\left[\frac{-2R^3}{(R+\varepsilon)^3}-1\right]a_1=-\rho_o B_o \tag{17a}$$

$$\Rightarrow\ a_1=\frac{\rho_o B_o}{3}, \tag{17b}$$

yielding the solution for the buoyancy perturbation pressure:

$$p_b(r,\theta)=\begin{cases}\dfrac{\rho_o B_o}{3}r\cos\theta, & r\le R\\[2ex] \dfrac{\rho_o B_o R^3}{3}\dfrac{\cos\theta}{r^2}, & r\ge R\end{cases}. \tag{18}$$

From Eq. (5), the effective buoyancy field readily follows:

$$\beta(\mathbf{r})=\begin{cases}\dfrac{2B_o}{3}, & r<R\\[2ex] \dfrac{B_o R^3}{3}\dfrac{(3\cos^2\theta-1)}{r^3}, & r>R\end{cases}. \tag{19}$$

This analytical expression for $\beta(\mathbf{r})$ is a main result of this paper and is plotted in the center panel of Fig. 1. Note the presence of $P_2(\cos\theta)$ in Eq. (19), with characteristic lobes evident in Fig. 1. Furthermore, setting $\theta=\pi/2$ in Eq. (19) yields a horizontal profile of β: the sphere itself accelerates vertically at $(2/3)B_o$, while the immediately adjacent environment subsides at $-(1/3)B$. This subsidence acceleration then decays fairly rapidly as r^{-3}.

One implication of these results is that the negative acceleration associated with near-field compensating subsidence is comparable in magnitude to the acceleration of the anomaly itself. This environmental acceleration declines rapidly with distance, yielding after finite time a descent of environmental air that is strongly enhanced near the anomaly. In a stably stratified environment (i.e., $d\theta/dz>0$), such a distribution of descent yields a corresponding distribution of positive buoyancy anomalies that then generate their own convection and cause this chain to repeat itself. This is, of course, simply a description of how gravity waves propagate away from rising fluid, and we see that the horizontal inhomogeneity of the environmental acceleration evident in Fig. 1 is critical to this propagation.

For completeness, we also note that the environmental fluid's horizontal acceleration can be computed as

$$\frac{D\mathbf{u}}{Dt}=-\frac{1}{\rho_o}\nabla_h p_b=\frac{B_o R^3 z}{(x^2+y^2+z^2)^{5/2}}(x,y). \tag{20}$$

The environmental fluid above $z=0$ accelerates outward and is displaced away from the sphere, while the fluid beneath $z=0$ accelerates inward to fill the vacated space as depicted in Fig. 1c.

4. Buoyant motion from rest

What is the relevance of the foregoing results? For a buoyancy anomaly accelerating from rest in a quiescent environment, the dynamic pressure is zero and the effective buoyancy gives the full Lagrangian acceleration. The motion will stay buoyancy dominated until enough momentum has developed that the dynamic pressure force can no longer be neglected.

Since the length of the thermal $L_{\rm th}$ is the only length in the problem, it sets the length scale of the buoyancy-dominated motion. The end of this regime occurs when $\nabla p_b\sim\nabla p_d$. Noting that $\nabla p_d\sim\rho W^2/L_{\rm th}$ and $\nabla p_b\sim\rho B_o$ as a result of Poisson's equations, we have the following

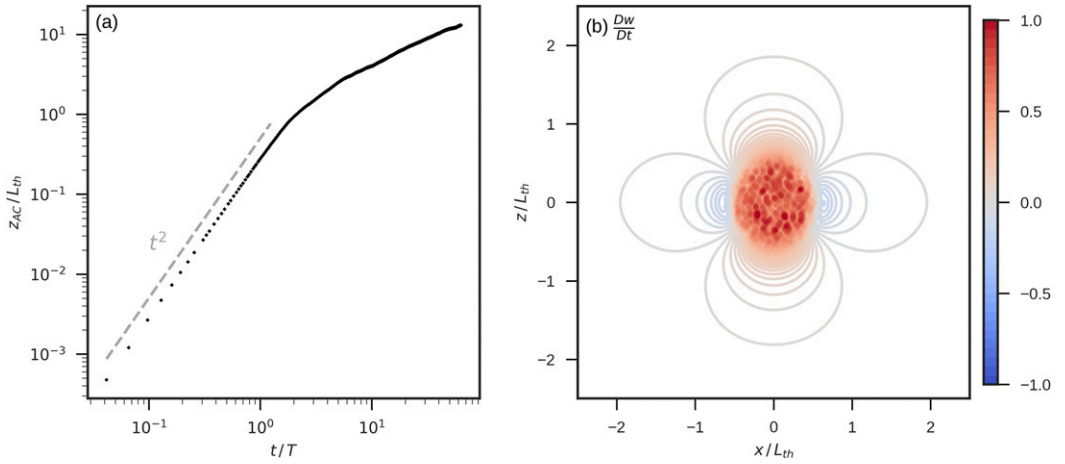

FIG. 2. (a) Log–log plot of the height of the anomaly vs time, and (b) contour plot of the initial Lagrangian acceleration.

scalings for the buoyancy-dominated regime's duration and final velocity:

$$\tau \sim \sqrt{\frac{L_{\text{th}}}{B_o}}, \tag{21}$$

$$W \sim \sqrt{B_o L_{\text{th}}}. \tag{22}$$

During this buoyancy-dominated regime, a spherical thermal has near-uniform effective buoyancy and thus achieves solid-body motion with $\Delta z \approx (1/2)\beta t^2$.

For a representative thermal with $L_{\text{th}} \sim 0.5$ km (Romps and Charn 2015; Hernandez-Deckers and Sherwood 2016), this parabolic motion would describe a thermal's rise through a typical boundary layer. With buoyancy in the characteristic range of $B = 0.01$–$0.1\ \text{m s}^{-2}$, the scaling yields $W_b \sim 2$–$7\ \text{m s}^{-1}$, which is in close agreement with velocities observed for thermals in numerical studies (Romps and Charn 2015; Hernandez-Deckers and Sherwood 2016). The above scalings are also in consonance with the idealized model for a spherical thermal put forward by Escudier and Maxworthy (1973), who under several assumptions (e.g., that the thermal's motion is detrainment free, drag from dynamic pressure is negligible, and the entrainment of ambient fluid is proportional to surface area and velocity) obtained asymptotic solutions for the thermal's trajectory.

To validate this account of the buoyancy-dominated motion, we analyze the direct numerical simulations of a spherical thermal conducted in Lecoanet and Jeevanjee (2018) using Dedalus,[1] an open-source pseudospectral framework (Burns et al. 2016). As detailed in appendix A, we solve the nondimensional Boussinesq equations for the turbulent motion of a heterogeneous density anomaly rising through a neutrally stratified environment.

As shown in Fig. 2b, the spatial structure of the instantaneous Lagrangian acceleration from rest matches the analytical β result of Eq. (19) (displayed in Fig. 1). Let angle brackets denote an average over the thermal's initial spherical volume. We find that $\langle\beta\rangle/\langle B\rangle = 0.65$, which is in close agreement with the theoretical prediction of 2/3.

To verify the length scale of the buoyancy-dominated regime, we track the center of the density anomaly through time by computing

$$\mathbf{x}_{\text{AC}}(t) = \frac{\int_\Omega \rho'(t)\mathbf{x}\, dV}{\int_\Omega \rho'(t)\, dV}, \tag{23}$$

where Ω is the full domain. As shown in Fig. 2a, the buoyancy-dominated regime, characterized by $\Delta z \sim \beta t^2$ ascent, persists until the thermal rises a distance comparable to the thermal's own length, validating the analytical scaling of Eq. (22).

5. Effective buoyancy of a mature thermal

After the initial motion chronicled in the prior section, the thermal transitions to a turbulent regime distinguished by a "vortex ring" circulation. This structure, which loosely resembles the laminar Hill's vortex, consists of an ellipsoidal thermal that encases a rotating ring of more anomalous density; fluid ascends in the ring's interior and descends on the periphery (Scorer 1957; Woodward 1959).

[1] For more information and links to the source code, see http://dedalus-project.org/.

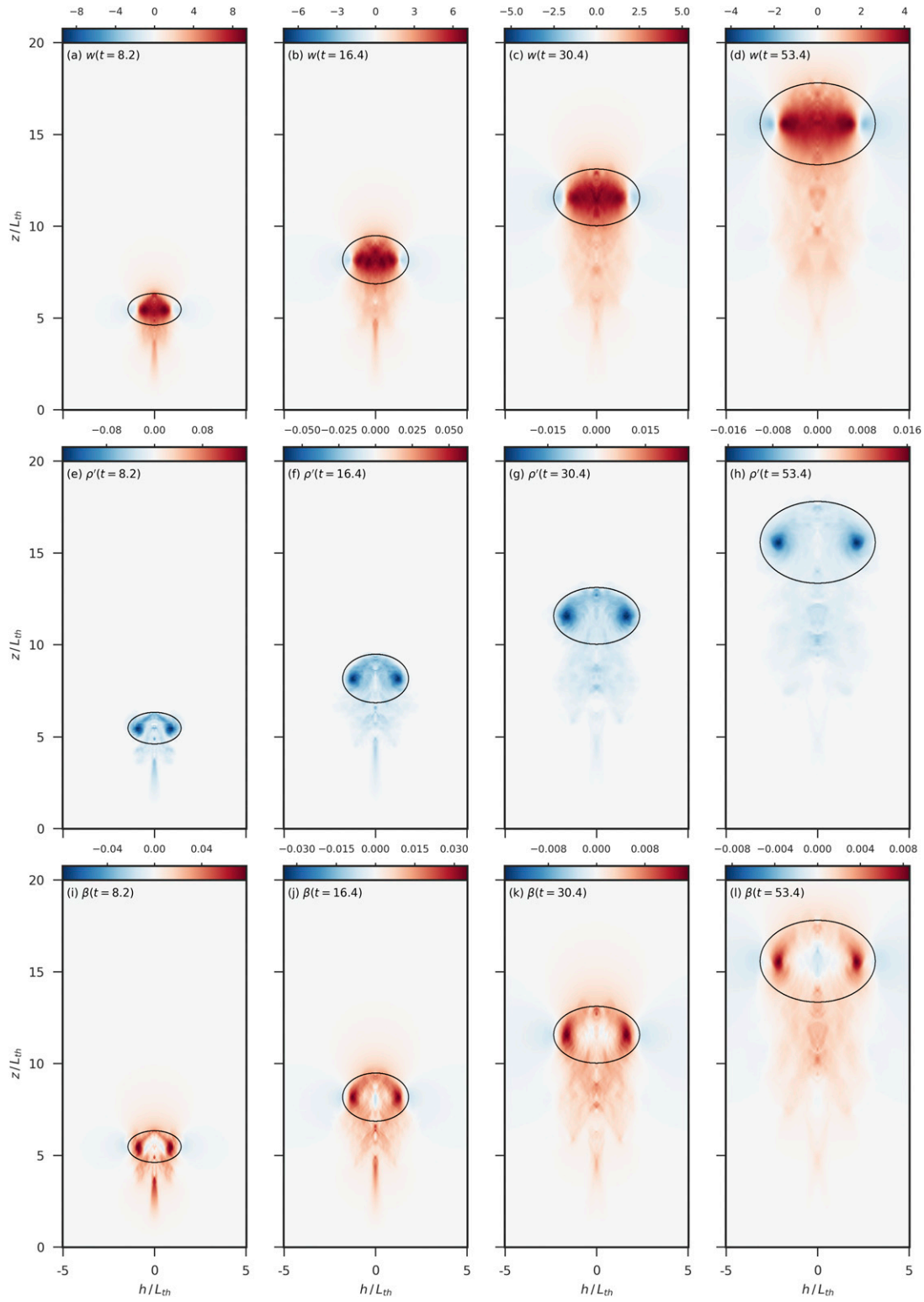

FIG. 3. Evolution of the azimuthally averaged (a)–(d) w, (e)–(h) ρ', and (i)–(l) β fields. Black contours show the identified boundaries of the actively convecting ellipsoidal thermals.

Figure 3 demonstrates azimuthally averaged w, ρ', and β fields for the ellipsoidal mature thermal. The β distribution is found using the Poisson solver detailed in Jeevanjee and Romps (2015). We observe that β also is nonuniform in the thermal's interior: the concentration of buoyant fluid in the ring imposes a secondary structure with a pattern akin to the superposition of two buoyant spheres. Accordingly, β is enhanced over the ring and of opposite sign in the center. We find that the presence of this ring of relatively undiluted fluid depends on the level of turbulence in our simulations. More laminar simulations in Lecoanet and Jeevanjee (2018) find a much stronger ring. Considering that thermals in the atmosphere are far more turbulent than our simulations, this suggests that the β field is closer to uniform in real thermals.

Motivated by the findings of the prior section, we examine to what extent the mean β of a mature thermal may be explained by considering a uniformly buoyant ellipsoid. With that goal in mind, we first derive the effective buoyancy of an ellipsoid via exploiting a mathematical equivalence between effective buoyancy and the equations of magnetostatics.

a. *Magnetostatics correspondence*

Understanding the connection between magnetostatics and effective buoyancy requires familiarity with the concept of magnetization, which we outline below. Readers are referred to Griffiths (2017) and Jackson (1998) for a thorough treatment of the topic.

Consider a small circular loop of wire through which a steady current flows. If the loop has vector area $\mathbf{a}$ and carries current I, then taking $\mathbf{a} \to 0$ while fixing the *dipole moment* $\mathbf{m} = \mathbf{a}I$ yields the *dipole magnetic field*. This miniature loop circuit is a conceptual model for the magnetic dipole moments generated by atomic electrons. A physical magnet is composed of many such dipole moments aligned in a common direction and described by the magnetic dipole moment per unit volume, known as the *magnetization*, $\mathbf{M} = d\mathbf{m}/dV$. Inside a magnet that is uniformly magnetized in the vertical, we would have $\mathbf{M} = M_o \mathbf{e}_z$.

We will consider the case of a permanently magnetized object, where the interior dipoles are aligned even in the absence of external magnetic fields. The total magnetic field $\mathbf{B}$ resulting from the magnet's permanent dipoles is found by first accomplishing the mathematically simpler task of determining the auxiliary $\mathbf{H}$ field, defined as

$$\mathbf{H} = \frac{\mathbf{B}}{\mu_0} - \mathbf{M}. \tag{24}$$

In the absence of any free currents (i.e., currents following through wires), the curl and divergence of the above definition give

$$\nabla \times \mathbf{H} = 0, \tag{25}$$

$$\nabla \cdot \mathbf{H} = -\nabla \cdot \mathbf{M}. \tag{26}$$

Since $\mathbf{H}$ is curl free, Helmholtz's theorem tells us that $\mathbf{H} = -\nabla \Phi_M$, where Φ_M is a scalar function known as the magnetic potential. We then have the Poisson's equation

$$\nabla^2 \Phi_M = \nabla \cdot \mathbf{M}. \tag{27}$$

We regard $\nabla \cdot \mathbf{M}$ as the "bound magnetic charge," which is nonzero only on the surface of the magnetized object. If the magnet is magnetized only in the vertical, then

$$\nabla^2 \Phi_M = \frac{\partial \mathbf{M}}{\partial z}. \tag{28}$$

This equation is mathematically equivalent to Eq. (4a), the Poisson's equation for the buoyancy perturbation pressure. In addition, Φ_M and p_b share identical boundary conditions: both must be finite at the origin, vanish at ∞, and continuous over the boundary of a magnetic/fluid body.

This mathematical equivalence spells out the following correspondence:

$$\begin{aligned} &\text{Fluid} \quad \text{Magnetostatics} \\ &B \leftrightarrow M \\ &\frac{p_b}{\rho_o} \leftrightarrow \Phi_M \\ &-\frac{\nabla p_b}{\rho_o} \leftrightarrow \mathbf{H} \\ &\beta \leftrightarrow \frac{\mathbf{B}}{\mu_0}. \end{aligned} \tag{29}$$

The effective buoyancy of an arbitrarily shaped fluid anomaly is mathematically equivalent to the magnetic field generated by a vertically magnetized body of the same shape.

The classical theory of magnetized bodies is replete with analytical results. Poisson is attributed with finding the magnetic field inside a uniformly magnetized sphere, and Maxwell gives the corresponding result for an ellipsoid in article 437 of Maxwell (1873). A modern treatment of the magnetic field inside a magnetized ellipsoid can be found in Stoner (1945), and Tejedor et al. (1995) derives formulas for the external magnetic field presented in the following section.

The magnetostatics correspondence also clarifies the relationship between effective buoyancy and induced mass. We have shown that a spherical buoyancy anomaly *accelerates uniformly*, moving as if it were a solid body. This explains why its induced mass is equal to that of a solid sphere, and why the spatial structure of β in Eq. (19) is identical to that of the potential flow of a solid sphere translating at a steady velocity $U\mathbf{e}_z$ in an infinite fluid

[Batchelor 2000; simply let the buoyant sphere evolve for time Δt and set $U = (2B_o/3)\Delta t$]. For an ellipsoid, the effective buoyancy result presented in the next section also agrees with the induced mass formulas computed in articles 114 and 373 of Lamb (1945). Does an arbitrarily shaped density anomaly also have a uniform effective buoyancy and thus exactly mimic its solid-body counterparts?

Again, we turn to the magnetostatics literature. The effective buoyancy is uniform only if ∇p_b is uniform in the fluid anomaly's interior. In article 437 Maxwell (1873) proved that **H**—the magnetostatics quantity analogous to ∇p_b—is uniform in a magnetized body's interior only if the body's surface is quadratic, the only closed finite quadratic surface being the ellipsoid. Therefore, we conclude that only *ellipsoidal* bodies have uniform β and thus have induced mass coefficients equal to their solid-body counterparts.

b. Ellipsoidal thermal

Consider an azimuthally symmetric ellipsoidal density anomaly of uniform Archimedean buoyancy B_o and specified by major axes (W, W, H). Let $\alpha = W/H$ be the aspect ratio of the ellipsoid with $\alpha < 1$ indicating a prolate ellipsoid and $\alpha > 1$ an oblate ellipsoid. Adapting the corresponding result for the magnetized ellipsoid presented in article 437 of Maxwell (1873) and fully derived in Stoner (1945), the buoyancy perturbation pressure in the interior of the ellipsoid takes the form

$$p_b = f(\alpha)\rho_o B_o z, \tag{30}$$

where we have defined

$$f(\alpha) = \begin{cases} \dfrac{\alpha^2}{1-\alpha^2}\left[\dfrac{\log\left(\dfrac{1+\sqrt{1-\alpha^2}}{\alpha}\right)}{\sqrt{1-\alpha^2}} - 1\right], & \alpha < 1 \\ \dfrac{1}{3}, & \alpha = 1 \\ \dfrac{\alpha^2}{1-\alpha^2}\left[1 - \dfrac{1}{\sqrt{\alpha^2-1}}\sin^{-1}\left(\dfrac{\sqrt{\alpha^2-1}}{\alpha}\right)\right], & \alpha > 1 \end{cases}. \tag{31}$$

Note that the oblate formula ($\alpha > 1$) can be obtained by taking the real part of the prolate formula ($\alpha < 1$) and applying the identity $\sin^{-1}x = -i\ln(\sqrt{1-x^2} + ix)$. For reference, $f(\alpha)$ corresponds to the demagnetization factor $D(\mu)$ of Eq. (4.2) in Stoner (1945) with $\alpha = \mu$.

As in the subcase of the sphere, p_b is a linear function of z inside the anomaly, and thus the whole ellipsoid uniformly accelerates in the vertical with an effective buoyancy of

$$\beta_{\text{ellipsoid}}(\alpha) = [1 - f(\alpha)]B_o, \tag{32}$$

as shown in Fig. 4. This formula is the quantitative foundation for the observation of Houze (2014) that wide pancake-shaped thermals are severely inhibited by their environment with $\beta \approx 0$, while narrow pencil-shaped anomalies impart negligible momentum to their environment, yielding $\beta \approx B$.

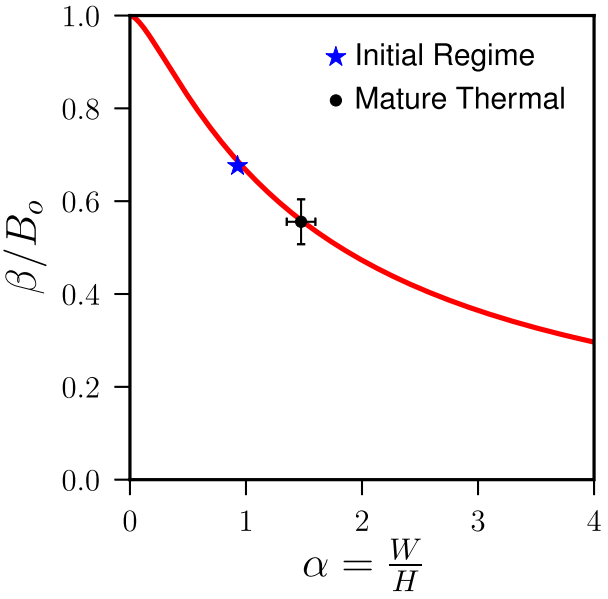

FIG. 4. Comparison between β averaged over the ellipsoidal thermal as a function of the diagnosed aspect ratio and the analytical formula [Eq. (32)]. Thermal identification was conducted every $0.1T$, yielding 5 snapshots of the initial regime and 70 snapshots of the mature thermal. Bars indicate the standard deviation of the data for each regime (error bars for the initial regime are smaller than the marker).

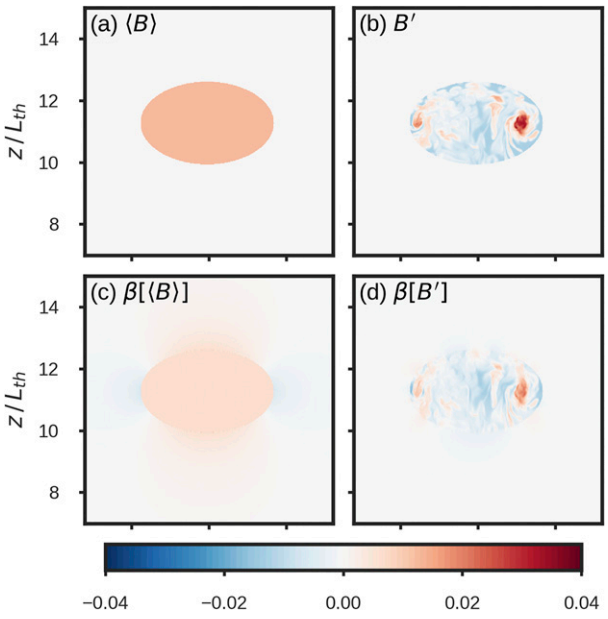

FIG. 5. (a) Vertical cross section at $t = 28.7$ of the volume average of the thermal's Archimedean buoyancy $\langle B\rangle$, (b) the departures from the mean ellipsoidal buoyancy $B' = B - \langle B\rangle$, (c) effective buoyancy generated by $\langle B\rangle$ distribution, and (d) effective buoyancy generated by B' distribution. See text for discussion.

Importantly, it also enables us to move beyond the limiting cases and understand the regime relevant for atmospheric thermals. Hernandez-Deckers and Sherwood (2016) found evidence for slightly prolate thermals, while Scorer (1957), Woodward (1959), and Damiani et al. (2006) observe moderately oblate thermals consistent with our simulations, which have $\alpha \approx 1.4$.

c. *Comparison to simulation*

Equipped with the idealized solution [Eq. (32)], we investigate its potential relevance to the simulated ellipsoidal thermals. Rigorous comparison to the simulation results requires introducing an objective method to identify the thermal's boundary. To achieve this, we implement a simple ρ'-based approach as described in appendix B. Example identification results are shown in Fig. 3.

Thermal identification enables us to compute the volume average of β over the thermal, again denoted as $\langle\beta\rangle$. Figure 4 compares $\langle\beta\rangle/\langle B\rangle$ to the analytical result of Eq. (32), evaluated with the thermal's aspect ratio. The analytical curve is found to accurately explain the effective buoyancy over the mature thermal's ascent. In particular, the time-mean $\langle\beta\rangle$ of the turbulent thermal is within $0.01B_o$ of the analytical result—a remarkable agreement. This finding allows us to go beyond scaling arguments and make a first analytical step toward rigorously understanding the forces acting on a turbulent thermal.

A lingering question, however, is, Why do we find such close agreement despite the heterogeneous ring structure present in the B field? Consider decomposing the thermal's Archimedean buoyancy field according to $B = \langle B\rangle + B'$. By definition, we have that $\langle B'\rangle = 0$, and thus B' contains opposite-signed regions that cancel when averaged over the thermal. Taking advantage of the linearity of Poisson's equation, β admits the decomposition $\beta = \beta[\langle B\rangle] + \beta[B']$, where $\beta[\langle B\rangle]$ is the effective buoyancy generated by a uniform ellipsoid of constant Archimedean buoyancy $\langle B\rangle$. Likewise, $\beta[B']$ is the effective buoyancy resulting from the heterogeneous B' field. See Fig. 5 for a plot of these quantities. As expected, $\beta[\langle B\rangle]$ is constant in the ellipsoid and is described by the analytical result of the prior section.

We observe that the $\beta[B']$ field inherits the heterogeneous features of the B' field and preserves the distribution of opposite-signed regions. As a consequence, if we average $\beta[B']$ over the thermal, then cancellation between the opposite-signed regions yields a value three orders of magnitude smaller than $\beta[\langle B\rangle]$. Therefore, we find that the departures from $\langle B\rangle$ make a negligible contribution to $\langle\beta\rangle$, supplying the agreement observed in Fig. 4.

6. Discussion

Our main findings are as follows:

- There exists an exact correspondence between magnetostatics and the fluid dynamics of effective buoyancy [Eq. (29)].
- This correspondence supplies an analytical formula for the effective buoyancy of spherical and ellipsoidal anomalies—the only fluid geometries that experience a uniform buoyant acceleration, and thus have virtual mass coefficients identical to their solid-body counterparts.
- The effective buoyancy of a heterogeneous turbulent thermal is captured by an analytical function of the thermal's aspect ratio (Fig. 4).

The above results enable the computation of a turbulent thermal's buoyant acceleration from the coarse geometry of the density field, and thus can be applied to lower-resolution observational or model data. Another application of these results is to cumulus parameterizations, and specifically those that parameterize the vertical velocity equation. As summarized by Roode et al. (2012), a wide range of virtual mass coefficients are employed in the literature. However, the results presented here, and in particular Fig. 4, suggest that the virtual mass coefficients that are much different from 2/3 are not justified by thermal-based reasoning.

A limitation of this study is that our simulations do not account for water vapor or a stratified environment. This poses a problem, however, only if a "wet" thermal in a

stratified fluid deviates from the coarse ellipsoidal geometry necessary to apply our analysis. Fortunately, atmospheric observations (Damiani et al. 2006) and wet stratified simulations (Sherwood et al. 2013; Romps and Charn 2015; Hernandez-Deckers and Sherwood 2016) find thermals that possess the necessary ellipsoidal shape.

Note that our analysis emphasized the buoyancy perturbation pressure, but the dynamic pressure force is equally important to the circulation of an ellipsoidal vortex ring. While there has been recent progress in visualizing and parameterizing the dynamic pressure force (Peters 2016), a deeper quantitative understanding is still lacking. In particular, we would benefit from analytical solutions to Eq. (4b) that reveal the dynamic pressure's spatial pattern and mean effect on a mature thermal. Future research should aim to address these questions.

Acknowledgments. NT thanks Kirk McDonald for the discussion of the magnetostatics content and for bringing Maxwell's proof to his attention. The authors thank three anonymous reviewers in addition to Howard Stone, Aaron Match, and David Romps for the helpful discussions and feedback. NJ is supported by a Harry Hess fellowship from the Princeton Geosciences Department. DL is supported by a PCTS fellowship and a Lyman Spitzer Jr. fellowship. Computations were conducted with support by the NASA High-End Computing (HEC) Program through the NASA Advanced Supercomputing (NAS) Division at Ames Research Center on Pleiades with allocations GID s1647 and s1439.

APPENDIX A

Simulation

We briefly outline the details of the simulations and refer readers to Lecoanet and Jeevanjee (2018, their section 2) for a complete treatment. We nondimensionalize according to $\hat{\mathbf{x}} = \mathbf{x}/L_{\rm th}$, $\hat{\mathbf{v}} = \mathbf{v}/V_{\rm th}$, and $\widehat{\rho'} = \rho'/\alpha\Delta T$, where the thermal has characteristic length $L_{\rm th}$, velocity $V_{\rm th}$, and anomalous density $\alpha\Delta T$ (here, α is the coefficient ofthermal expansion). Nondimensionalizing the Boussinesq equations provides the definition of the thermal's characteristic velocity,

$$V_{\rm th} = \sqrt{\frac{gL_{\rm th}\alpha\Delta T}{\rho_o}}. \tag{A1}$$

The solution to the nondimensional equations is then completely described by the Reynold's number,

$$\mathrm{Re} = \frac{V_{\rm th}L_{\rm th}}{\nu}, \tag{A2}$$

and the Prandtl number,

$$\mathrm{Pr} = \frac{\kappa}{\nu}, \tag{A3}$$

where κ is the thermal diffusivity. We take $\mathrm{Pr} = 1$ and $\mathrm{Re} = 2/\sqrt{10} \times 10^4 \approx 6300$.

To resolve the small-scale features of the initial acceleration field shown in Fig. 2b, we initialize the sphere in the center of a cubic domain of length $5L_{\rm th}$ and represent the solution with $(1024)^3$ Fourier modes. To simulate the ascent of a mature thermal, we initialize the sphere above the bottom of a rectangular domain of height $20L_{\rm th}$ and horizontal extent $10L_{\rm th}$, and use 512 modes in the horizontal directions and 1024 modes in the vertical direction.

The spherical anomaly is seeded with a random heterogeneous $\widehat{\rho'}$ distribution such that the average of $\widehat{\rho'}$ over the sphere is -1. In the smaller domain (larger domain) simulation, the root-mean-square of $\widehat{\rho'}$ is 0.48 (0.21). Both simulations are run until the anomaly collides with the top of the domain. In the larger domain simulation, analysis was conducted on the thermal's ascent (shown in Fig. 3) from $z = 6L_{\rm th}$ to $z = 16L_{\rm th}$, during which the thermal exhibits ellipsoidal vortex motion and does not interact with the domain top.

APPENDIX B

Thermal Tracking

To minimize complexity we solve for the ellipsoidal thermal volume by identifying the major axes of an azimuthally symmetric ellipsoid via a fixed threshold on the azimuthally averaged density anomaly field $\rho'(h, z)$, where $h = \sqrt{x^2 + y^2}$ is the horizontal radial coordinate.

We first locate the central vertical axis of the thermal by performing a vertical velocity-weighted average of (x, y) on each vertical level. After computing the azimuthal average of $\rho'(h, z)$ about this central axis, we reduce the dimensionality again by vertically averaging $\rho'(h, z)$ over each column to yield $\overline{\rho'}(h)$ and separately averaging $\rho'(h, z)$ across each row to give $\overline{\rho'}(z)$. Both averages are shown in Fig. B1.

The extent of the ellipsoid's vertical axis is set by the height above the ellipsoid's center where $\overline{\rho'}(z)$ is reduced by 85% from its maximum value. Likewise, the horizontal axis is set by the radial distance at which $\overline{\rho'}(h)$ is reduced by 85% from its maximum value. To minimize subjectivity, we conduct a sensitivity analysis and identify the ellipsoid with alternate choices of an 80% and a 90% reduction threshold. Figure B1 reveals that identification results are robust to variations of the ρ'

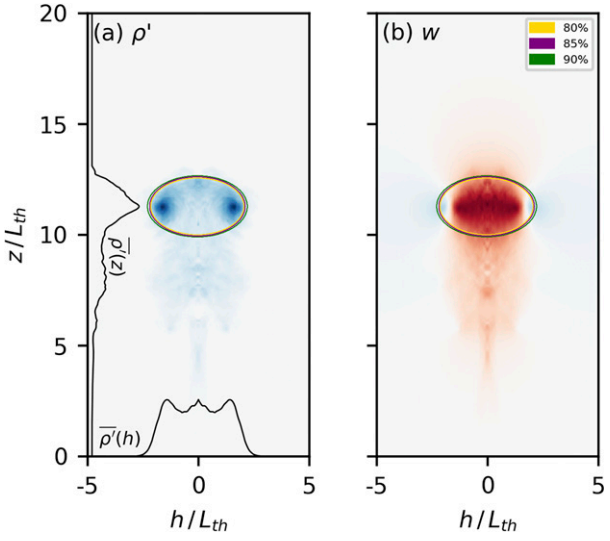

FIG. B1. The azimuthally averaged (a) ρ' and (b) w fields at t = 28.7 with identified ellipsoidal boundaries corresponding to 80%, 85%, and 90% reduction thresholds of $|\rho'|$. The column-averaged $\overline{\rho'}(h)$ and row-averaged $\overline{\rho'}(z)$ are also shown.

threshold. More sophisticated thermal tracking methods exist (e.g., Romps and Charn 2015), but we believe this rudimentary algorithm does a sufficient job of detecting the prominent ellipsoidal structure of the thermal.

REFERENCES

Batchelor, G. K., 2000: *An Introduction to Fluid Dynamics*. Cambridge Mathematical Library, Cambridge University Press, 615 pp.

Burns, K., G. Vasil, J. Oishi, D. Lecoanet, and B. Brown, 2016: Dedalus: Flexible framework for spectrally solving differential equations. Astrophysics Source Code Library, http://adsabs.harvard.edu/abs/2016ascl.soft03015B.

Damiani, R., and G. Vali, 2007: Evidence for tilted toroidal circulations in cumulus. *J. Atmos. Sci.*, **64**, 2045–2060, https://doi.org/10.1175/JAS3941.1.

——, ——, and S. Haimov, 2006: The structure of thermals in cumulus from airborne dual-Doppler radar observations. *J. Atmos. Sci.*, **63**, 1432–1450, https://doi.org/10.1175/JAS3701.1.

Davies-Jones, R., 2003: An expression for effective buoyancy in surroundings with horizontal density gradients. *J. Atmos. Sci.*, **60**, 2922–2925, https://doi.org/10.1175/1520-0469(2003)060<2922:AEFEBI>2.0.CO;2.

De Roode, S. R., A. P. Siebesma, H. J. J. Jonker, and Y. D. Voogd, 2012: Parameterization of the vertical velocity equation for shallow cumulus clouds. *Mon. Wea. Rev.*, **140**, 2424–2436, https://doi.org/10.1175/MWR-D-11-00277.1.

Doswell, C. A., and P. M. Markowski, 2004: Is buoyancy a relative quantity? *Mon. Wea. Rev.*, **132**, 853–863, https://doi.org/10.1175/1520-0493(2004)132<0853:IBARQ>2.0.CO;2.

Escudier, M. P., and T. Maxworthy, 1973: On the motion of turbulent thermals. *J. Fluid Mech.*, **61**, 541–552, https://doi.org/10.1017/S0022112073000856.

Griffiths, D. J., 2017: *Introduction to Electrodynamics*. 4th ed. Cambridge University Press, 599 pp.

Hernandez-Deckers, D., and S. C. Sherwood, 2016: A numerical investigation of cumulus thermals. *J. Atmos. Sci.*, **73**, 4117–4136, https://doi.org/10.1175/JAS-D-15-0385.1.

Houze, R. A., Jr., 2014: *Cloud Dynamics*. 2nd ed. International Geophysics Series, Vol. 104, Academic Press, 432 pp.

Jackson, J. D., 1998: *Classical Electrodynamics*. 3rd ed. Wiley, 832 pp.

Jeevanjee, N., 2017: Vertical velocity in the gray zone. *J. Adv. Model. Earth Syst.*, **9**, 2304–2316, https://doi.org/10.1002/2017MS001059.

——, and D. M. Romps, 2015: Effective buoyancy, inertial pressure, and the mechanical generation of boundary layer mass flux by cold pools. *J. Atmos. Sci.*, **72**, 3199–3213, https://doi.org/10.1175/JAS-D-14-0349.1.

——, and ——, 2016: Effective buoyancy at the surface and aloft. *Quart. J. Roy. Meteor. Soc.*, **142**, 811–820, https://doi.org/10.1002/qj.2683.

Krueger, S. K., G. T. Mclean, and Q. Fu, 1995: Numerical simulation of the stratus-to-cumulus transition in the subtropical marine boundary layer. Part II: Boundary-layer circulation. *J. Atmos. Sci.*, **52**, 2851–2868, https://doi.org/10.1175/1520-0469(1995)052<2851:NSOTST>2.0.CO;2.

Lamb, H., 1945: *Hydrodynamics*. 6th ed. Dover, 738 pp.

Lecoanet, D., and N. Jeevanjee, 2018: Entrainment in resolved, turbulent dry thermals. arXiv.org, 11 pp., https://arxiv.org/abs/1804.09326v1.

Markowski, P., and Y. Richardson, 2011: *Mesoscale Meteorology in Midlatitudes*. Advancing Weather and Climate Science, John Wiley & Sons, 424 pp.

Maxwell, J. C., 1873: *Treatise on Electricity and Magnetism*. Vol. 2. Clarendon Press, 444 pp.

Morrison, H., 2016a: Impacts of updraft size and dimensionality on the perturbation pressure and vertical velocity in cumulus convection. Part I: Simple, generalized analytic solutions. *J. Atmos. Sci.*, **73**, 1441–1454, https://doi.org/10.1175/JAS-D-15-0040.1.

——, 2016b: Impacts of updraft size and dimensionality on the perturbation pressure and vertical velocity in cumulus convection. Part II: Comparison of theoretical and numerical solutions and fully dynamical simulations. *J. Atmos. Sci.*, **73**, 1455–1480, https://doi.org/10.1175/JAS-D-15-0041.1.

Pauluis, O., and S. Garner, 2006: Sensitivity of radiative–convective equilibrium simulations to horizontal resolution. *J. Atmos. Sci.*, **63**, 1910–1923, https://doi.org/10.1175/JAS3705.1.

Peters, J. M., 2016: The impact of effective buoyancy and dynamic pressure forcing on vertical velocities within two-dimensional updrafts. *J. Atmos. Sci.*, **73**, 4531–4551, https://doi.org/10.1175/JAS-D-16-0016.1.

Romps, D. M., and A. B. Charn, 2015: Sticky thermals: Evidence for a dominant balance between buoyancy and drag in cloud updrafts. *J. Atmos. Sci.*, **72**, 2890–2901, https://doi.org/10.1175/JAS-D-15-0042.1.

——, and Z. Kuang, 2010: Do undiluted convective plumes exist in the upper tropical troposphere? *J. Atmos. Sci.*, **67**, 468–484, https://doi.org/10.1175/2009JAS3184.1.

Scorer, R. S., 1957: Experiments on convection of isolated masses of buoyant fluid. *J. Fluid Mech.*, **2**, 583, https://doi.org/10.1017/S0022112057000397.

Sherwood, S. C., D. Hernàndez-Deckers, M. Colin, and F. Robinson, 2013: Slippery thermals and the cumulus entrainment paradox. *J. Atmos. Sci.*, **70**, 2426–2442, https://doi.org/10.1175/JAS-D-12-0220.1.

Stoner, E. C., 1945: XCVII. The demagnetizing factors for ellipsoids. *London Edinburgh Dublin Philos. Mag. J. Sci.*, **36**, 803–821, https://doi.org/10.1080/14786444508521510.

Tejedor, M., H. Rubio, L. Elbaile, and R. Iglesias, 1995: External fields created by uniformly magnetized ellipsoids and spheroids. *IEEE Trans. Magn.*, **31**, 830–836, https://doi.org/10.1109/20.364589.

Turner, J. S., 1964: The dynamics of spheroidal masses of buoyant fluid. *J. Fluid Mech.*, **19**, 481–490, https://doi.org/10.1017/S0022112064000854.

Weisman, M. L., W. C. Skamarock, and J. B. Klemp, 1997: The resolution dependence of explicitly modeled convective systems. *Mon. Wea. Rev.*, **125**, 527–548, https://doi.org/10.1175/1520-0493(1997)125<0527:TRDOEM>2.0.CO;2.

Woodward, B., 1959: The motion in and around isolated thermals. *Quart. J. Roy. Meteor. Soc.*, **85**, 144–151, https://doi.org/10.1002/qj.49708536407.

Xu, K.-M., and D. A. Randall, 2001: Updraft and downdraft statistics of simulated tropical and midlatitude cumulus convection. *J. Atmos. Sci.*, **58**, 1630–1649, https://doi.org/10.1175/1520-0469(2001)058<1630:UADSOS>2.0.CO;2.